



# Ni Doped $Zn_3P_2$ Nanoparticles: Synthesis, Structural, Optical, and Magnetic Properties

Nakka Praveenkumar<sup>1</sup> · Madhusudhana Rao N.<sup>1</sup>

Received: 1 August 2023 / Accepted: 11 December 2023 / Published online: 22 December 2023  
© The Author(s), under exclusive licence to Springer Science+Business Media, LLC, part of Springer Nature 2023

## Abstract

Dilute magnetic semiconductor nanoparticles of zinc phosphide ( $Zn_{3-x}Ni_xP_2$ ), doped with nickel, were synthesized using a solid-state reaction method. The doping levels of nickel were varied at  $x=0.01, 0.03, 0.05,$  and  $0.07$ . The study investigated the influence of varying nickel dopant concentrations on the structural, optical, and magnetic characteristics of the synthesized materials. Based on the XRD investigation, it is evident that the generated samples have a tetragonal structure, with no discernible presence of additional nickel or any other contaminants in the diffraction peaks. The lattice parameters exhibited a positive correlation with the Ni content, indicating that an increase in Ni concentration led to an increase in lattice parameters. SEM pictures provided empirical evidence supporting the notion that the dimensions of the nanoparticles exhibited a positive correlation with the extent of dopant incorporation. EDS examination indicates that the concentration of dopants closely approximates the desired atomic ratio. The optical band gap of the  $Zn_{3-x}Ni_xP_2$  nanoparticles exhibited a rise in value, namely from 1.410 to 1.433 eV, as the quantity of nickel was increased. The study revealed that photoluminescence emission peaks were consistently seen at nearly identical places, despite variations in excitation wavelengths. Additionally, it was noted that the strength of the emission peaks exhibited slight fluctuations, which were more pronounced as the concentration of the dopant rose. The study of the VSM data demonstrates a positive correlation between saturation magnetization and the Ni content, indicating that an increase in the Ni concentration leads to an increase in saturation magnetization.

**Keywords** Diluted magnetic semiconductor · Vacuum annealing furnace · Ni-doped  $Zn_3P_2$  nanoparticles · Room temperature ferromagnetism · B-H hysteresis loop

## 1 Introduction

Dilute magnetic semiconductors (DMS) have proven to be particularly advantageous in the field of spintronics, a specialized domain within nanoscale electronics that focuses on the manipulation and regulation of electron spin. The detection of spin is accomplished through the observation of the magnetic moment, which can be oriented either in an “up” or “down” configuration. Spintronics technology is founded upon the intrinsic spin characteristic of electrons, which has spurred much investigation in both theoretical and experimental domains [1]. Every DMS material possesses unique properties and potential uses in magneto-optical and magneto-transport systems [2]. Dilute magnetic

semiconductors are occasionally referred to as semi-magnetic semiconductors (SMSCs). In the realm of semiconductors, several significant definitions can be identified. A magnetic semiconductor refers to the ordered arrangement of magnetic constituents, while a dilute magnetic semiconductor denotes an alloy composed of both magnetic and nonmagnetic constituents. DMS materials offer numerous advantages, including enhanced speed, the ability to store data in compact spaces, improved resistance, and reduced power usage. The presence of magnetic characteristics was detected in both doped and undoped  $E^{2+}$  materials, specifically those composed of chalcogenides and oxides [3]. The aforementioned compounds exhibit limited semiconducting properties and possess relatively low Curie temperatures. The discovery of ferromagnetism in Mn-doped IV–VI [4], III–V [5], and II–VI [6] dilute magnetic semiconductors has significantly contributed to the advancement of spintronic applications. Ferromagnetic semiconductors (FM) possessing a Curie temperature ( $T_c$ ) exceeding 300 K represent the

✉ Madhusudhana Rao N.  
drnmrao@gmail.com

<sup>1</sup> Department of Physics, School of Advanced Sciences, VIT-AP University, Andhra Pradesh-522237, India

essential prerequisite in spintronics applications. The Zener model has been utilized to establish the presence of ferromagnetism at room temperature in Zinc-blende ferromagnetic semiconductors [7]. Diluted magnetic semiconductor (DMS) materials have gained significant attention in contemporary research. Notably, certain DMS materials have been found to have ferromagnetic properties even at ambient temperatures, as documented in the existing literature review on DMS materials. The majority of research efforts have focused on investigating numerous types of DMS compounds, employing diverse methodologies to elucidate their structural, optoelectrical, and magnetic characteristics. Transition elements have been included into DMS (dilute magnetic semiconductor) materials. Several instances of this include the doping of Cr in ZnTe [8], Sn in ZnS [9], Mn in InAs [10], Cr in AIP [11], Co in TiO<sub>2</sub> [12], and Ni in SnO<sub>2</sub> [13]. Historically, the research on II–V dilute magnetic semiconductors has been very limited compared to the more extensively studied II–VI, III–V, and IV–VI compound dilute magnetic semiconductors. The materials derived from DMS can be classified into three significant types, namely II–VI, IV–VI, and III–V, which are commonly referred to as dilute magnetic semiconductors. Upon introducing transition metals (Mn, Fe, Ni, V) and rare earth metals (Gd, Dy) as dopants, the nonmagnetic semiconductor material undergoes a transformation, resulting in the acquisition of magnetic properties.

This study discusses zinc phosphide (Zn<sub>3</sub>P<sub>2</sub>), which belongs to the class II–V of semiconducting materials. It is characterized as an earth-abundant, environmentally benign, polar, mixed-valent, and cost-effective semiconductor. Zinc phosphide is characterized as a diamagnetic substance and is classified as a p-type semiconducting material. It can be easily fabricated into thin films and nanoparticles, showcasing remarkable promise for solar applications. The material under consideration is a direct band-gap semiconductor, possessing a band gap that is well-suited for the development of single-junction solar cells. Specifically, the energy gap (E<sub>g</sub>) of this material is approximately 1.5 eV [14]. The P42/nmc space group (No.137) is observed in the primitive tetragonal crystal structure of zinc phosphide (Zn<sub>3</sub>P<sub>2</sub>) [15]. The material has a significantly high optical absorption coefficient, ranging from 10<sup>4</sup> to 10<sup>5</sup> cm<sup>-1</sup>, as well as a substantial carrier diffusion length of around 13 × 10<sup>6</sup> m [16]. The scientific community has shown significant interest in studying the characteristics of zinc phosphide in the context of thin-film photovoltaic cell advancement and its potential uses in solar energy research, as seen by the extensive coverage in academic literature. Currently, there has been significant research conducted in recent years to explore the enhancement of half-metallic ferromagnetism and magnetic semiconductors. These investigations have primarily focused on experimental studies including nano phases [17,

18], bulk materials [19, 20], and thin films [21, 22]. In the previous literature study, it is evident that there has been limited research conducted on the utilization of zinc phosphide (Zn<sub>3</sub>P<sub>2</sub>) material in conjunction with various dopants such as Ti-doped Zn<sub>3</sub>P<sub>2</sub> [23], Fe-doped Zn<sub>3</sub>P<sub>2</sub> [24], and Q-doped Zn<sub>3</sub>P<sub>2</sub> with different elements (Q = V, Cr, Mn, Fe, Co) [25]. These reviews were subsequently followed by ab initio studies. Zn<sub>3</sub>P<sub>2</sub> is classified as a semiconductor belonging to the II–V group compounds. This compound has been investigated in the literature review alongside other compounds from the same group, such as Ti-doped Cd<sub>3</sub>P<sub>2</sub> [26], Mn-doped ZnAs<sub>2</sub> [27], Mn-doped Zn<sub>3</sub>As<sub>2</sub> [28], and Mn-doped Cd<sub>3</sub>As<sub>2</sub> [29]. These studies have primarily focused on the electronic structural properties, magnetic properties, and half-metallic properties of Zn<sub>3</sub>P<sub>2</sub> using ab initio methods. Based on the conducted literature survey, it is possible to anticipate the utilization of several experimental techniques to investigate the structural, optical, and magnetic characteristics of transition elements doped with zinc phosphide (Zn<sub>3</sub>P<sub>2</sub>) compound.

In this study, the synthesis of nickel-doped zinc phosphide (Zn<sub>3</sub>P<sub>2</sub>) nanoparticles was carried out utilizing the conventional solid-state reaction approach. This method is considered highly effective for synthesizing nanoparticles due to its efficient and time-saving synthesis procedure, resulting in the formation of nanoparticles with excellent crystallinity. The inquiry will involve reporting on the effects of various nickel doping concentrations ( $x=0.00, 0.01, 0.03, 0.05, \text{ and } 0.07$ ) in the substitution of zinc atoms. The focus will be on analyzing the structural, optical, and magnetic properties of the resulting materials. The findings presented in this study hold significant value in the context of advancing materials for spintronics applications.

## 2 Experimental Details

### 2.1 Synthesis

The synthesis of nickel-doped zinc phosphide nanoparticles was conducted using the conventional solid-state reaction technique. Four samples with varying nickel concentrations were synthesized, denoted as N1 ( $x=0.01$ ), N2 ( $x=0.03$ ), N3 ( $x=0.05$ ), and N4 ( $x=0.07$ ). Zinc phosphide (Zn<sub>3</sub>P<sub>2</sub>) and nickel phosphide (Ni<sub>2</sub>P) are two chemical compounds that have been procured by the Sigma Aldrich corporation. Both of these substances are in the form of powders. All chemical reagents utilized in the study were of analytical purity and sourced from Sigma Aldrich. The compounds were measured based on a stoichiometric ratio of Zn<sub>3-x</sub>Ni<sub>x</sub>P<sub>2</sub>, where  $x$  values of 0.01, 0.03, 0.05, and 0.07 were used. The microbalance was utilized to prepare 3 g for each sample doped with nickel. Zinc phosphide (Zn<sub>3</sub>P<sub>2</sub>) is a substance known

for its hazardous properties, thus necessitating cautious handling during the fabrication of samples. To mitigate potential risks, it is recommended to employ an agate mortar and pestle for this purpose. To initiate the cleaning process, employ acetone to cleanse the mortar and pestle. The zinc phosphide and nickel phosphide compounds were subjected to extensive grinding for a duration of approximately 16 h. After the completion of the grinding process on pure material, it was found that dopant ions exhibited a tendency to aggregate in close proximity to one another, resulting in a uniform and homogeneous distribution. The powdered materials were placed into an alumina crucible using a fixed plate. The processed samples are stored within a tubular furnace, according to appropriate conditions. Each sample is maintained at a temperature of 500 °C for a duration of 5 h, while being subjected to a vacuum pressure of  $2 \times 10^{-2}$  mbar. Following the heating process, the nickel-doped samples were meticulously ground prior to undergoing characterization. The resultant outcome of the incorporation of nickel into zinc phosphide nanoparticles exhibited a black hue.

## 2.2 Characterizations

The primary objective of this study was to conduct several characterizations, including the utilization of X-ray diffraction (XRD) with the Rigaku-mini flex-600 instrument. XRD was employed to determine the crystalline structure of nanoparticles, utilizing Cu K $\alpha$  radiation with a wavelength of 1.5406 Å. The elemental composition was identified using energy dispersive X-ray analysis (EDAX) spectroscopy, and surface morphology was analyzed using scanning electron microscopy (SEM) with the JSM-IT 500 instrument. The optical band gap and diffused reflectance spectra were measured using Ultraviolet–visible near-infrared radiation spectroscopy (UV–vis-NIR) with the Perkin lambda 365 instrument. photoluminescence spectroscopy (PL) measurements were conducted using a Fluorescence spectrum (FP-8300) to analyze the emission characteristics at various excitation wavelengths, specifically 210 nm, 215 nm, 240 nm, and 307 nm. The saturation magnetization, coercivity, and retentivity were determined using a vibrating sample magnetometer (Lake Shore 7410 S).

## 3 Results and Discussion

### 3.1 Structural Properties

X-ray diffraction is widely recognized as a pivotal tool for characterizing materials, mostly due to its ability to discern the phase and crystallite size of a given substance. Figure 1a illustrates the X-ray diffraction patterns of nickel-doped zinc phosphide nanoparticles that were synthesized using

the conventional solid-state reaction approach. The X-ray diffraction patterns exhibit the presence of pure Zn<sub>3-x</sub>Ni<sub>x</sub>P<sub>2</sub> nanoparticles, where  $x$  represents the varying compositions of 0.00, 0.01, 0.03, 0.05, and 0.07. The X-ray diffraction pattern was examined in order to investigate the prominent peaks seen in both pure and doped samples, which displayed a distinct tetragonal structure of Zn<sub>3</sub>P<sub>2</sub>. The obtained results exhibit a precise match with the JCPDS cards (Reference NO. 74–1156), specifically in terms of the space group P42/nmc, which corresponds to space group number 137. The lattice parameter of zinc phosphide is characterized by equal values for the parameters  $a = b$  and  $c$ , which are both measured to be  $a = b = 8.0970$  Å. Additionally, the parameter  $c$  is determined to be 11.4500 Å. Furthermore, the angles  $\alpha$ ,  $\beta$ , and  $\gamma$  are all measured to be 90° (Based on JCPDS data). A comparable configuration was documented by I.K. El Zawawi et al. [30].

The diffraction peaks of pure and Ni-doped samples exhibit pronounced intensity and well-defined profiles, indicating the superior crystalline quality of zinc phosphide (Zn<sub>3</sub>P<sub>2</sub>) and its doped counterparts. Based on the findings depicted in Fig. 1a, it can be discerned that the X-ray diffraction pattern does not exhibit any additional peaks corresponding to dopant ions or other impurities. This observation suggests that the concentration of nickel doping has been effectively substituted inside the pure (Zn<sub>3</sub>P<sub>2</sub>) material. The X-ray diffraction pattern exhibited the presence of synthesized diffraction peaks at various angles. Specifically, the diffraction peaks were observed at angles of 23.36°, 25.82°, 26.98°, 29°, 31.45°, 32.24°, 34.14°, 36.74°, 40.94°, 43.16°, 44.8°, 53.06°, 55.7°, 61.26°, 62.32°, 65.14°, and 82.66°. These peaks corresponded to the diffraction indices (1 0 2), (2 1 1), (2 0 2), (2 1 2), (2 2 0), (2 0 3), (3 0 1), (3 0 2), (3 0 3), (3 2 2), (4 0 0), (4 2 2), (4 0 4), (4 0 5), (5 2 1), (4 4 0), and (6 2 4), respectively.

Figure 1b illustrates the fluctuations in the  $2\theta$  angle as the concentration of dopants increases in the pure sample. The observed alterations in the  $2\theta$  value can be attributed to the influence of Ni concentration. The variation in ionic radius between Zn<sup>+2</sup> (0.74 Å) and Ni<sup>+2</sup> (0.69 Å) on the lower side leads to a change in the angle  $2\theta$  towards the lower angle side as the concentration of nickel dopants increases from N1 to N4 samples. The ionic radius of the nickel dopant is smaller when compared to the pure element Zn<sup>+2</sup>. This smaller ionic radius of nickel allows for appropriate substitution in the pure combination. No papers regarding the comparison of Ni-doped Zn<sub>3</sub>P<sub>2</sub> nanoparticles were found. The study conducted by [31] observed comparable outcomes in the context of Dy-doped ZnO, with a shift towards the lower angle side. The intensity exhibited a reduction as the quantity of nickel dopant increased, ranging from N1 to N4 samples. The similarity in strength among the nickel doping levels derived from

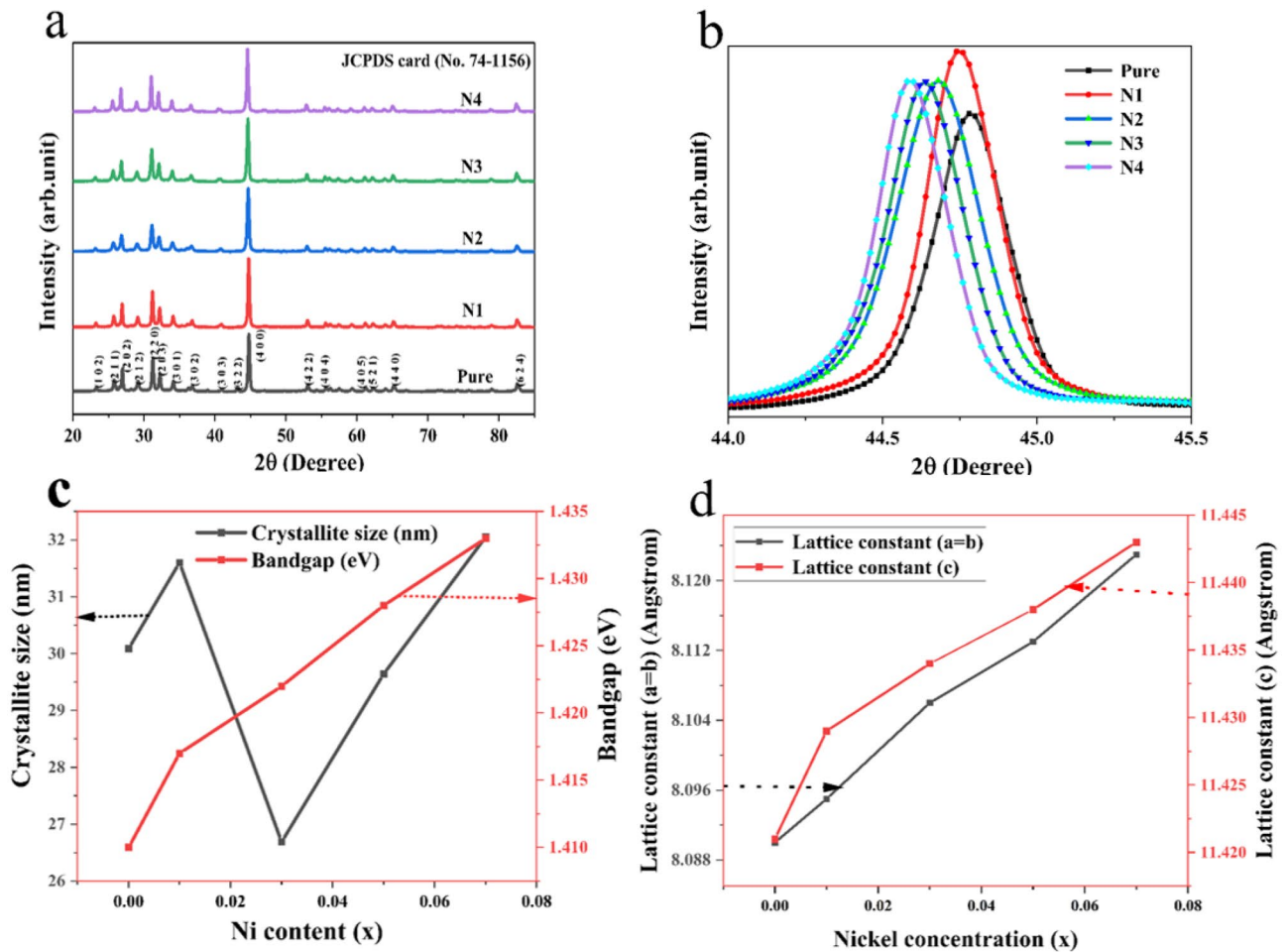


**Fig. 1** **a** XRD patterns of pure and  $Zn_{3-x}Ni_xP_2$  nanoparticles in the  $2\theta$  range of 20 to 85°. **b** Plane (4 0 0) of diffraction angle recording range of 44.0–45.5°. **c** Variation of crystallite size (D) and band gap (eV). **d** Variation of lattice parameters

N2, N3, and N4 concentrations is evident. No publications were found about the comparison of intensity. However, Kuppan et al. [32] discussed that in their study on Ni-doped  $SnO_2$  powder samples, the peak intensity exhibited a reduction as the nickel concentration increased. Figure 1c shows the variation in crystallite size and optical

band gap. The increase in Ni concentration from N2 to N4 samples resulted in an observed increase in crystallite size, as depicted in Table 1. The estimation of the average crystallite size (D) for both Pure and all synthesized samples was conducted based on the (4 0 0) plane, utilizing the Debye Scherer equation [33].

**Table 1** Summary of angle ( $2\theta$ ), full width at half maximum (FWHM), crystallite size, lattice constant, micro-strain, dislocation density, and band gap of pure and Ni doped  $Zn_3P_2$  nanoparticles

System name	$2\theta$ (degree)	FWHM	Crystallite size D (nm)	a (Å)	c (Å)	Micro strain ( $10^{-3}$ )	Dislocation density ( $10^{15}$ ) $m^{-2}$	Bandgap (eV)
Pure	44.78	0.285	30.09	8.090	11.421	1.15	1.10	1.410
N1 (0.01)	44.74	0.271	31.60	8.095	11.429	1.10	1.00	1.417
N2 (0.03)	44.68	0.321	26.69	8.106	11.434	1.30	1.40	1.422
N3 (0.05)	44.64	0.289	29.64	8.113	11.438	1.17	1.13	1.428
N4 (0.07)	44.58	0.267	32.05	8.123	11.443	1.08	0.97	1.433

$$\text{Crystallite size } D = \frac{K\lambda}{\beta\cos\theta} \quad (1)$$

where  $D$  represents the average crystallite size derived from the dominant peak of both the pure and doped samples, and  $K$  denotes the constant with its respective value. The variable  $K$  is assigned a value of 0.9. The symbol  $\lambda$  represents the wavelength of X-ray diffraction, specifically  $CuK\alpha$  with a value of 0.15406 nm.  $\beta$  denotes the full-width at half-maximum (FWHM) of a peak, both for a pure sample and a doped sample, specifically at the (4 0 0) position. Lastly,  $\theta$  represents the diffraction angle of the dominant peak at the (4 0 0) position.

The lattice parameters for pure and nickel-doped nanoparticles will be determined based on the tetragonal structure, utilizing the equation derived from the X-ray diffraction results.

$$\frac{1}{d^2} = \left( \frac{h^2 + k^2}{a^2} + \frac{l^2}{c^2} \right) \quad (2)$$

where  $h$ ,  $k$ , and  $l$  are the miller indices of (4 0 0) plane,  $d$  means interplanar spacing given by Bragg's law relation ( $n\lambda = 2d\sin\theta$ ) and  $d = n\lambda/2\sin\theta$ ,  $n$  is the order of the diffraction ( $n=1$ ),  $\lambda$  wavelength of incident ray ( $\lambda = 1.5406 \text{ \AA}$ ) and  $\theta$  be the angle of diffraction. The lattice parameters exhibited an increase as the Ni content rose, with the values of  $a=b$  and  $c$  changing from  $a=b=8.090 \text{ \AA}$   $c=11.421 \text{ \AA}$  to  $a=b=8.1238 \text{ \AA}$   $c=11.443 \text{ \AA}$  as shown in Fig. 1d. This phenomenon might perhaps be attributed to the development of internal stress inside the produced samples and variations in the ionic radius of Zn and Ni.

The dislocation density exhibited a reduction as the content of nickel increased in the prepared samples N2, N3, and N4, as seen in Table 1. The calculation of defects in the crystalline structure of both pure and Ni-doped samples involves the utilization of dislocation density ( $\delta$ ), which is defined as the reciprocal of the square of the average crystalline dimension ( $D$ ). This relationship is employed for the aforementioned purpose.

$$\text{Dislocation density } \delta = \frac{1}{D^2} \quad (3)$$

X-ray diffraction enables the examination of micro-strain phenomena such as bending, hardness, cracking, and similar characteristics. The micro-strain value exhibited a reduction when the Ni content increased from N2 to N4 samples, potentially indicating a relationship between the strain of the material and the observed trend. The micro-strain ( $\epsilon$ ) can be determined by employing the subsequent equation.

$$\text{Micro-strain } \epsilon = \frac{\beta\cos\theta}{4} \quad (4)$$

where  $\beta$  is the full-width half maximum (FWHM) for both pure and doped synthesized samples and  $\theta$  is the angle of diffraction (4 0 0) plane.

### 3.2 Elemental Studies

The elemental composition of  $Zn_{3-x}Ni_xP_2$  nanoparticles at different nickel concentrations (N1, N2, N3, and N4) can be analyzed by the utilization of Energy dispersive x-ray spectroscopy (EDS), as depicted in Fig. 2. The analysis of the spectra of  $Zn_3P_2$  samples doped with Ni revealed the presence of zinc (Zn), phosphorus (P), and nickel (Ni) in atomic ratios that closely matched the anticipated values. Based on the examination conducted using X-ray diffraction data and EDAX analysis, it was determined that no more impurities were detected. Furthermore, the substitution of Ni dopant ions in  $Zn_3P_2$  was shown to be successful. The observed results provided an indication of the level of purity shown by the nanoparticles of Ni-doped  $Zn_3P_2$ .

### 3.3 Surface Morphological Studies

Scanning electron microscopy (SEM) is widely regarded as a highly effective characterization tool for the analysis of material morphological structures. The investigation focused on the analysis of nanoparticles composed of zinc phosphide ( $Zn_3P_2$ ) that were doped with nickel. The study encompassed several concentrations of nickel, specifically N1, N2, N3, and N4 samples, as illustrated in Fig. 3. In SEM images, it was seen that the introduction of higher doping concentrations in the pure system resulted in a transformation of fine aggregates into larger aggregates, accompanied by the formation of spherical shapes.

The X-ray diffraction results indicate that the crystallite size is smaller when compared to the findings from the scanning electron microscopy (SEM) examination, as presented in Table 1. The extent of agglomeration is contingent upon the concentration of dopants, whereby an increase in dopant concentration leads to the displacement of atoms inside the pure molecule.

### 3.4 Optical Properties

The characterization of UV–vis–NIR spectrometers is a highly effective analytical approach for the assessment of optical properties. Two characteristics, namely absorption, and reflectance, can be measured. However, the reflectance data was seen. The optical characteristics of nanoparticles of zinc phosphide doped with nickel were examined using infrared (IR) spectra obtained using diffuse reflectance spectroscopy (DRS). Figure 4a displays the diffused reflectance spectra obtained at ambient temperature for both undoped and Ni-doped  $Zn_3P_2$  nanoparticles, encompassing

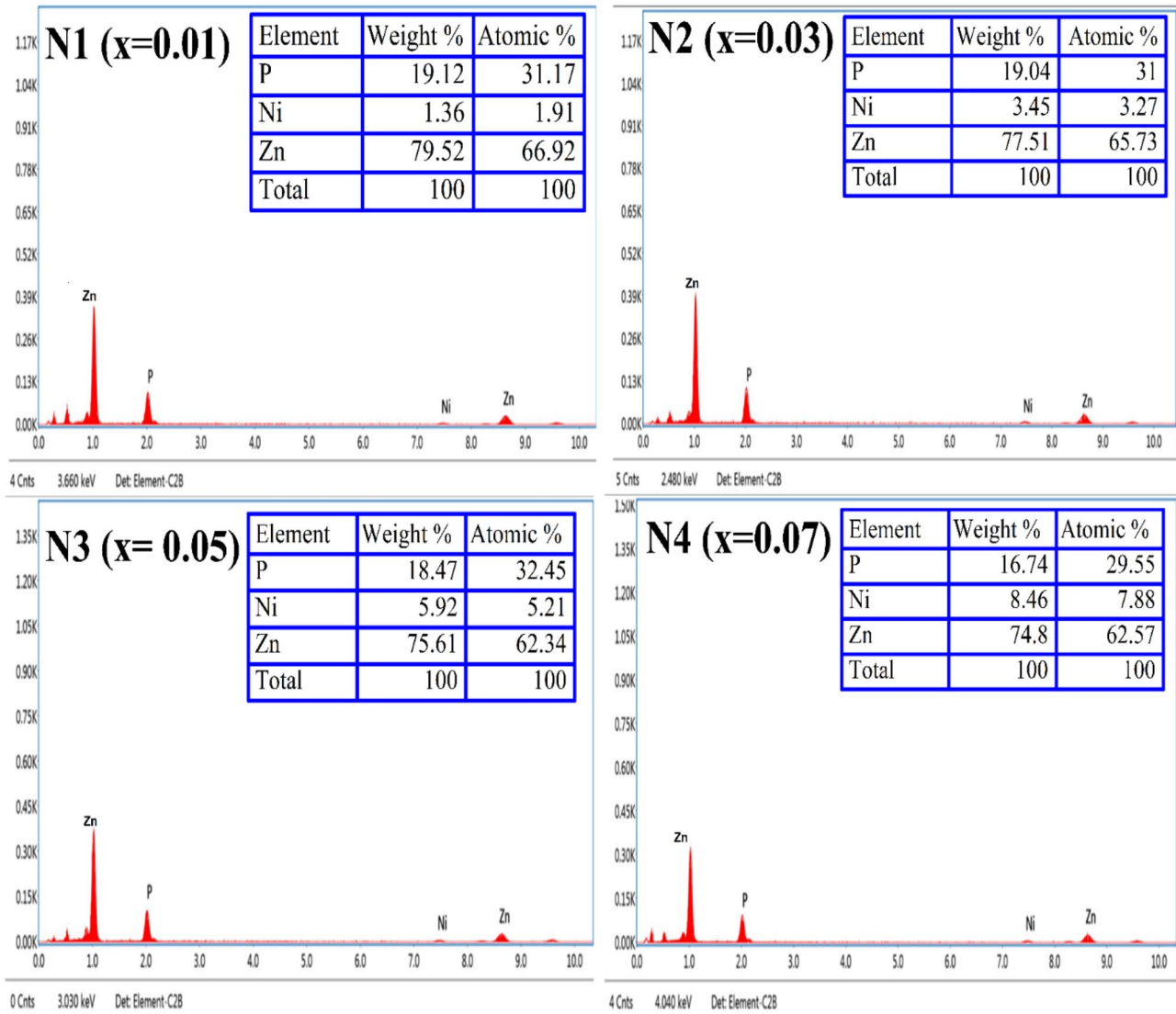


**Fig. 2** EDAX spectra of  $Zn_{3-x}Ni_xP_2$  nanoparticles

a wavelength range of 200 to 1100 nm, as specified from 400 to 1100 nm.

The Pure nanoparticles demonstrate a high level of reflection in the infrared (IR) region, but the zinc phosphide nanoparticles doped with nickel exhibit significantly lower reflectance in the same IR region. The reflectance of  $Zn_{3-x}Ni_xP_2$  nanoparticles increased when the nickel concentration increased from N1 to N4 samples within the infrared region.

The optical band gap of pure and all synthesized samples was calculated using the Tauc equation.

$$F(R).hv = A(hv - E_g)^n \quad (5)$$

The absorption coefficient ( $\alpha$ ) is denoted by  $F(R) = \alpha$ , where R represents the reflectance. The Kubelka–Munk function,  $F(R)$ , is a mathematical expression that is

connected to the absorption coefficient ( $\alpha$ ). The constant A and the constant  $h$  refer to Planck's constant, respectively. The value of Planck's constant is  $6.625 \times 10^{-34}$  J.s. In this context,  $h\nu$  represents the energy of a photon, while  $E_g$  denotes the optical band gap between the valence band and conduction band. Additionally, the parameter  $n$  assumes distinct values of  $1/2$ ,  $2$ ,  $3/2$ , and  $3$ , corresponding to direct transitions, indirect transitions, directly forbidden transitions, and indirect forbidden transitions, respectively. The value of the parameter “ $n$ ” is contingent upon the characteristics of the electron transition. Specifically, in the case of direct permitted transitions, the value of “ $n$ ” is chosen as  $1/2$ . Next, we can extend the linear portion of the absorption coefficient graph, where the value of  $\alpha$  is equal to zero, which was plotted as a function of the square of the product of  $F(R)$  and photon energy ( $h\nu$ ).

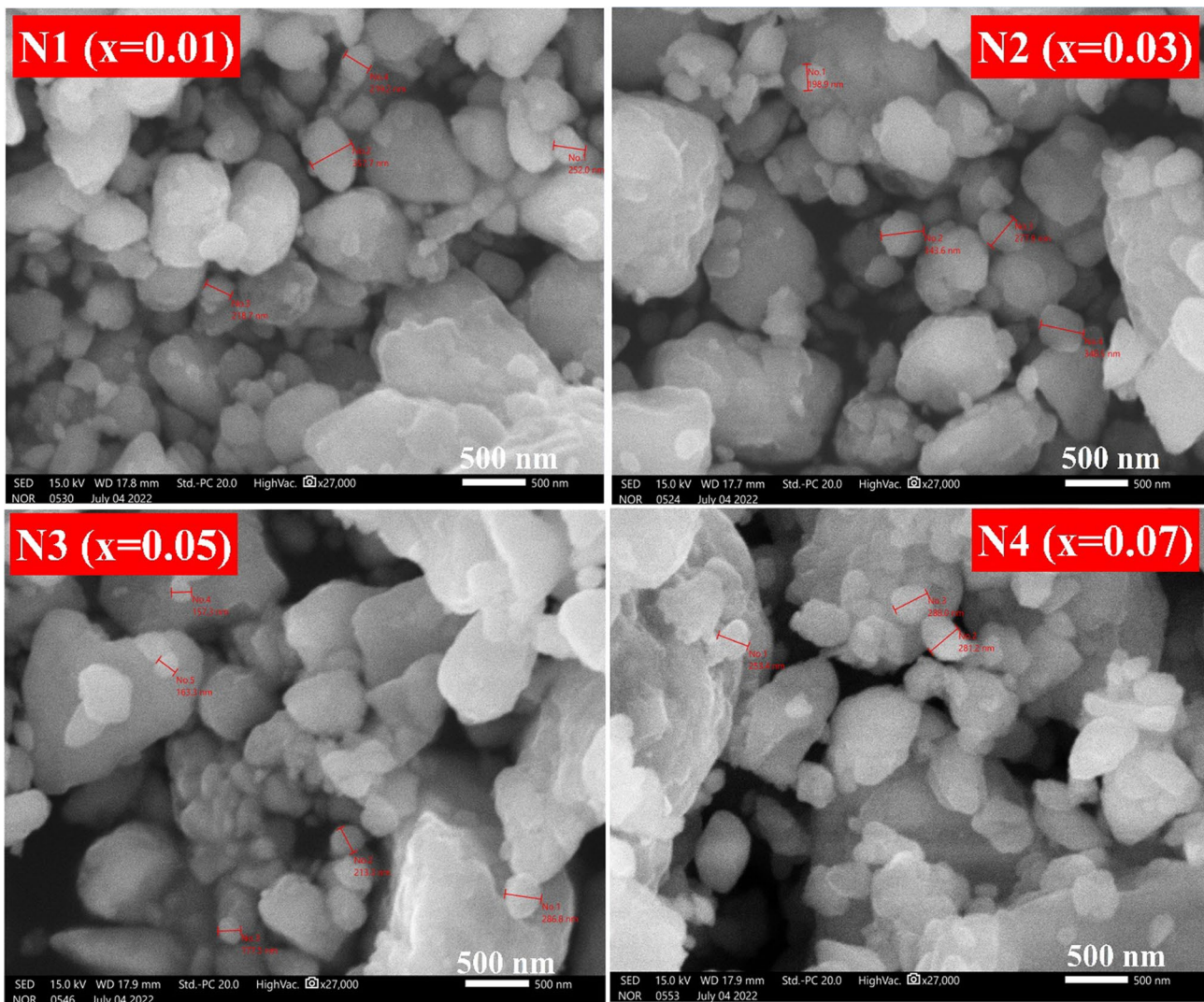


**Fig. 3** SEM images of Zn<sub>3-x</sub>Ni<sub>x</sub>P<sub>2</sub> nanoparticles in the range of 500 nm

The Kubelka–Munk function, denoted as  $F(R)$ , is determined by employing the subsequent equation for computational purposes.

$$F(R) = \frac{(1 - R)^2}{2R} \quad (6)$$

where  $R$  is the diffused reflectance and  $F(R)$  is the function of reflectance. Figure 4b illustrates the optical band gap values of the pure sample and Ni-doped samples N1, N2, N3, and N4 throughout the energy range of 1.35 to 1.55 eV. The researchers in a previous study [14] reported the observation of a 1.5 eV optical band gap in nanoparticles composed only of Zn<sub>3</sub>P<sub>2</sub>.

The optical band gap increases from 1.410 to 1.433 eV with increasing Ni content and is tabulated in Table 1. The rise in the optical band gap with increasing Ni content may

be related to the Burstein–Moss effect. As a result of the Fermi level migrating to the conduction band and occupying some of the lowest levels in the conduction band, the band gap widens, requiring more energy to move from the valance band to the conduction band. No instances of doping effects on a pristine (Zn<sub>3</sub>P<sub>2</sub>) system have been reported. However, it has been observed that when the system is annealed at 623 K and has a thickness of 483 nm, it exhibits an optical band gap of 1.56 eV [30]. The study conducted by [34] similarly observed an increase in bandgap in Ni-doped ZnS nanoparticles.

### 3.5 Photoluminescence Studies

The photoluminescence spectra of Ni-doped Zn<sub>3</sub>P<sub>2</sub> samples that were synthesized were seen at different excitation wavelengths, specifically 210 nm, 215 nm, 240 nm, and 307 nm,

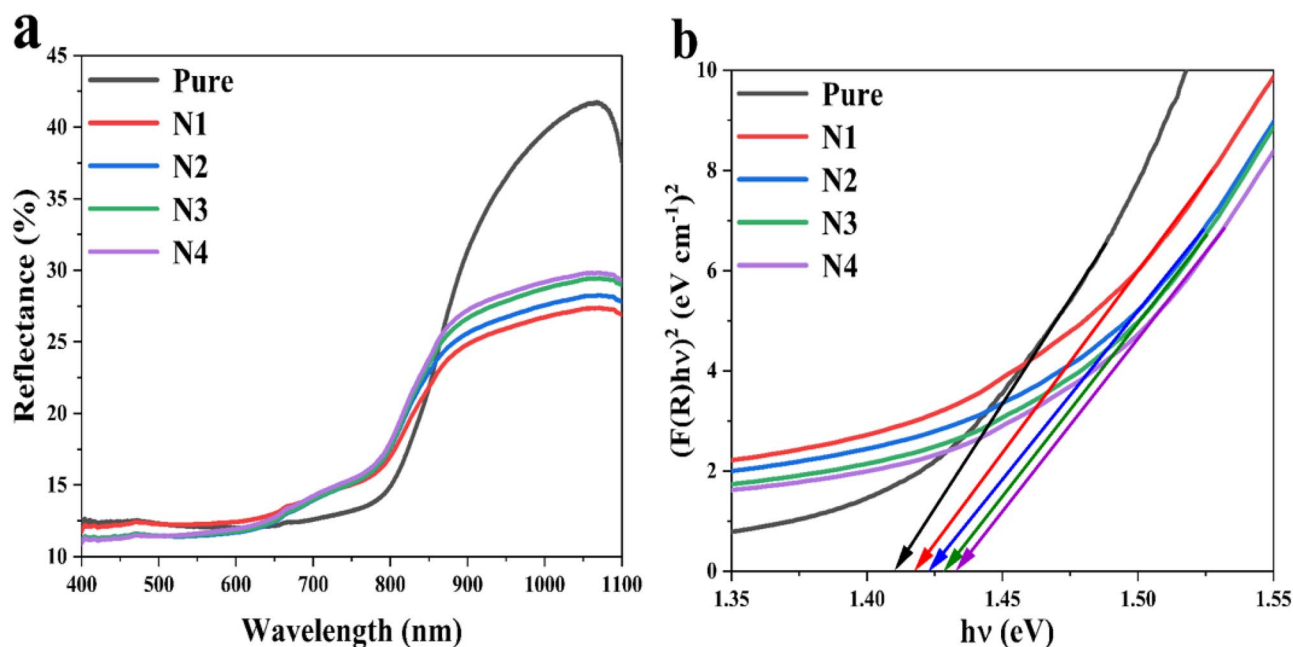


**Fig. 4** Diffused reflectance spectra of pure and  $\text{Zn}_{3-x}\text{Ni}_x\text{P}_2$  nanoparticles (a) and plot of  $(F(R)hv)^2$  versus  $h\nu$  of pure and Ni-doped  $\text{Zn}_3\text{P}_2$  nanoparticles (b)

as depicted in Fig. 5. Photoluminescence (PL) spectroscopy provides valuable insights into the characteristics of materials. The radiative recombination process and electronic band structure are commonly affected by flaws, which are highly sensitive to their performance. Contactless and non-destructive techniques are employed to characterize the optoelectronic properties of semiconductors (SC). The parameters of photoluminescence (PL) spectroscopic emission peaks, including concentrations and positions, are interconnected with the properties of defects or electronic bands [35]. Conduct a comprehensive examination of the pair transition in the photoluminescence (PL) spectra at low-temperature conditions, as documented in reference [36]. In order to examine the temperature variation ranging from 5.9 to 309 K [37], the emission peak of a polycrystalline  $\text{Zn}_3\text{P}_2$  wafer was analyzed. The temperature variations ranging from 14 to 350 K were examined in Ag-doped  $\text{Zn}_3\text{P}_2$  films [38]. The highest emission occurs at a wavelength of 460–545 nm and this emission is sustained at a temperature of 300 °C [39].

Figure 5a displays the photoluminescence (PL) spectra of nanoparticles of  $\text{Zn}_3\text{P}_2$  doped with Ni. The spectra were obtained using an excitation wavelength of 210 nm and a recorded wavelength range of 220 to 440 nm. Three distinct emission peaks may be observed in the ultraviolet area, specifically at wavelengths of 277 nm (4.47 eV), 301 nm (4.11 eV), and 324 nm (3.81 eV). The intensity exhibited a positive correlation with the nickel doping content, as observed in the transition from N1 to N4 samples. All emission peak points exhibit identical wavelength positions. The

presence of nickel does not have an impact on the peak shift observed in the pure matrix. The emission spectrum exhibited a prominent peak at a wavelength of 301 nm, indicating the highest intensity of emission. In contrast, a less intense emission band was found at a wavelength of 324 nm.

Figure 5b displays the photoluminescence (PL) spectra of  $\text{Zn}_{3-x}\text{Ni}_x\text{P}_2$  nanoparticles when excited at a wavelength of 215 nm. The measured wavelengths range from 220 to 400 nm. The presence of Ni-doped  $\text{Zn}_3\text{P}_2$  nanoparticles at different concentrations resulted in the observation of two distinct emission peaks. The first peak, observed at 238 nm (5.21 eV), exhibited ultraviolet coloration. The second peak, observed at 390 nm (3.17 eV), exhibited a violet coloration. The intensity exhibits a positive correlation with the progressive augmentation of dopant concentration, ranging from N1 to N4 samples. The emission peaks exhibit a nearly identical wavelength. The most prominent emission peak was detected at a wavelength of 390 nm, whereas a less intense emission band was identified at 238 nm.

Figure 5c illustrates the synthesis of the photoluminescence spectra (PL) of  $\text{Zn}_{3-x}\text{Ni}_x\text{P}_2$  nanoparticles at ambient temperature, wherein the nanoparticles are excited at a wavelength of 240 nm. The recorded range for the spectra spans from 250 to 700 nm. Nanoparticles of  $\text{Zn}_3\text{P}_2$  doped with Ni at varying concentrations exhibit distinct emission band peaks, namely ultraviolet region at 304 nm (4 eV), violet emission at 393 nm (3.15 eV), and two more peaks in the blue emission spectrum at 469 nm (2.64 eV) and 481 nm (2.57 eV). The emission band peak at 393 nm is the most



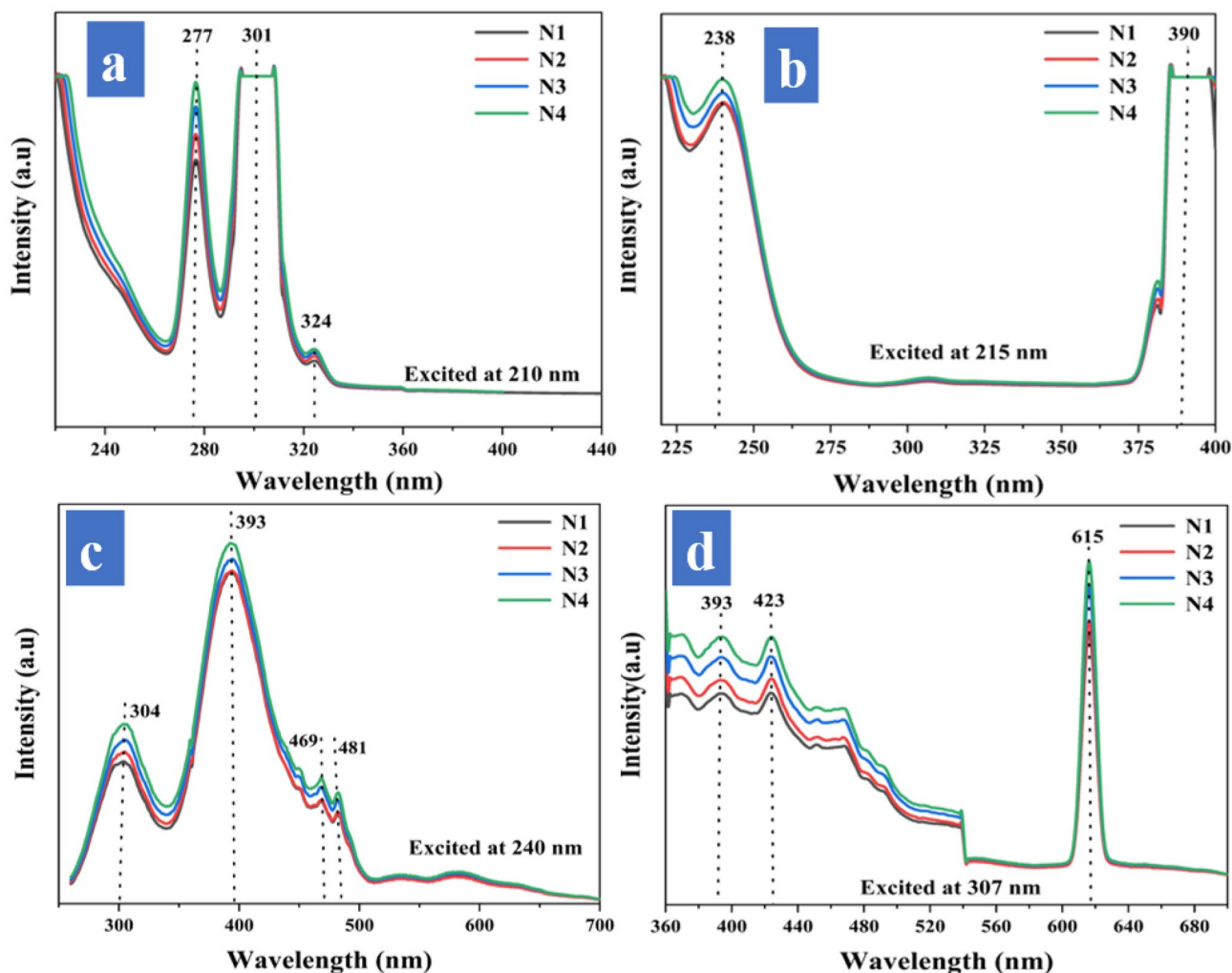


**Fig. 5** Photoluminescence spectra of  $Zn_{3-x}Ni_xP_2$  nanoparticles with different excitation wavelengths at 210 nm (a), 215 nm (b), 240 nm (c), and 370 nm (d)

intense in the violet emission zone. The intensity exhibited a positive correlation with the nickel concentrations, as observed in the N1 to N4 samples. The emission peaks of all synthesized nanoparticles exhibit a high degree of proximity, with a wavelength of around 393 nm. The emission spectrum exhibited a prominent peak at a wavelength of 393 nm, accompanied by three less intense bands at 304 nm, 469 nm, and 481 nm.

Figure 5d presents the results of synthesizing Ni-doped  $Zn_3P_2$  nanoparticles, which were subjected to an excitation wavelength of 307 nm. The reported wavelength range for these nanoparticles spanned from 360 to 700 nm. The observed rise in intensity from N1 to N4 samples can be attributed to the influence of nickel concentration. Additionally, the emission spectra revealed the presence of two violet bands at 393 nm (3.15 eV) and 423 nm (2.93 eV), as well as an orange emission at 615 nm (2 eV). The most prominent emission peak was detected at a wavelength of

615 nm, while two less intense bands were found at 393 nm and 423 nm.

The direct band gap of the zinc phosphide material is measured to be 1.5 eV. The band edge of the synthesized nanoparticles does not align with that of bulk  $Zn_3P_2$ , as illustrated in Fig. 5a–d. This could result from surface imperfections in nanoparticles, which cause shallow and deep traps below the conduction band [40]. No reference has been found for comparing the doped  $Zn_3P_2$  nanoparticles. However, G.Z. Shen et al. [41] have previously examined the properties of single crystalline trumpetlike zinc phosphide nanostructures, specifically focusing on the broad emission peak centered at 585 nm (2.1 eV) in their study. In their study, Tec Hock Lim et al. [42] examined the photoluminescence (PL) spectrum emission of  $\alpha$ - $Zn_3P_2$  particles dispersed in butanol and PL spectrum exhibited a peak centered at 470 nm (2.6 eV) for the  $\alpha$ - $Zn_3P_2$  particles, whereas the solvent showed a peak at 350 nm (3.5 eV). No reports have

been published about the comparison of photoluminescence (PL) in Ni-doped  $Zn_3P_2$  nanoparticles. In a previous study [43], the emission-centered peak at 384 nm (3.22 eV) was seen in Ni-doped ZnO thin films. The emission intensities at a wavelength of 382 nm exhibit a 5% rise when Ni-doped ZnO is utilized [44].

### 3.6 Magnetic Properties

Figure 6 illustrates the relationship between magnetization (B) and applied field (H) for  $Zn_{3-x}Ni_xP_2$  nanoparticles with varying nickel (Ni) concentrations (N1, N2, N3, and N4). The investigation was conducted at room temperature (RT) using a vibrating sample magnetometer (VSM). According to the hysteresis loop, the range of magnetic field strengths spans from  $-15,000$  to  $+15,000$  Oe. The main objective of

this study is to investigate the magnetic characteristics of  $Zn_3P_2$  samples doped with Ni. The VSM is now engaged in the study and application of Faraday's Law of Induction.

Figure 6a illustrates the magnetization against the magnetic field curve (M-H curve) of the undoped compound at ambient temperature, within the field range of  $-15,000$  to  $+15,000$  Oe. In theory, it can be postulated that the compound  $Zn_3P_2$  (II–V) has diamagnetic properties. The B-H graph illustrates that undoped  $Zn_3P_2$  demonstrates ferromagnetic behavior when it is produced at the nanoscale. In contrast to the diamagnetic properties exhibited by the stoichiometric bulk  $Zn_3P_2$ , the presence of ferromagnetic (FM) material within the diamagnetic lattice of the undoped  $Zn_3P_2$  combination could potentially account for this phenomenon. The presence of flaws or zinc vacancies may account for this phenomenon [45].

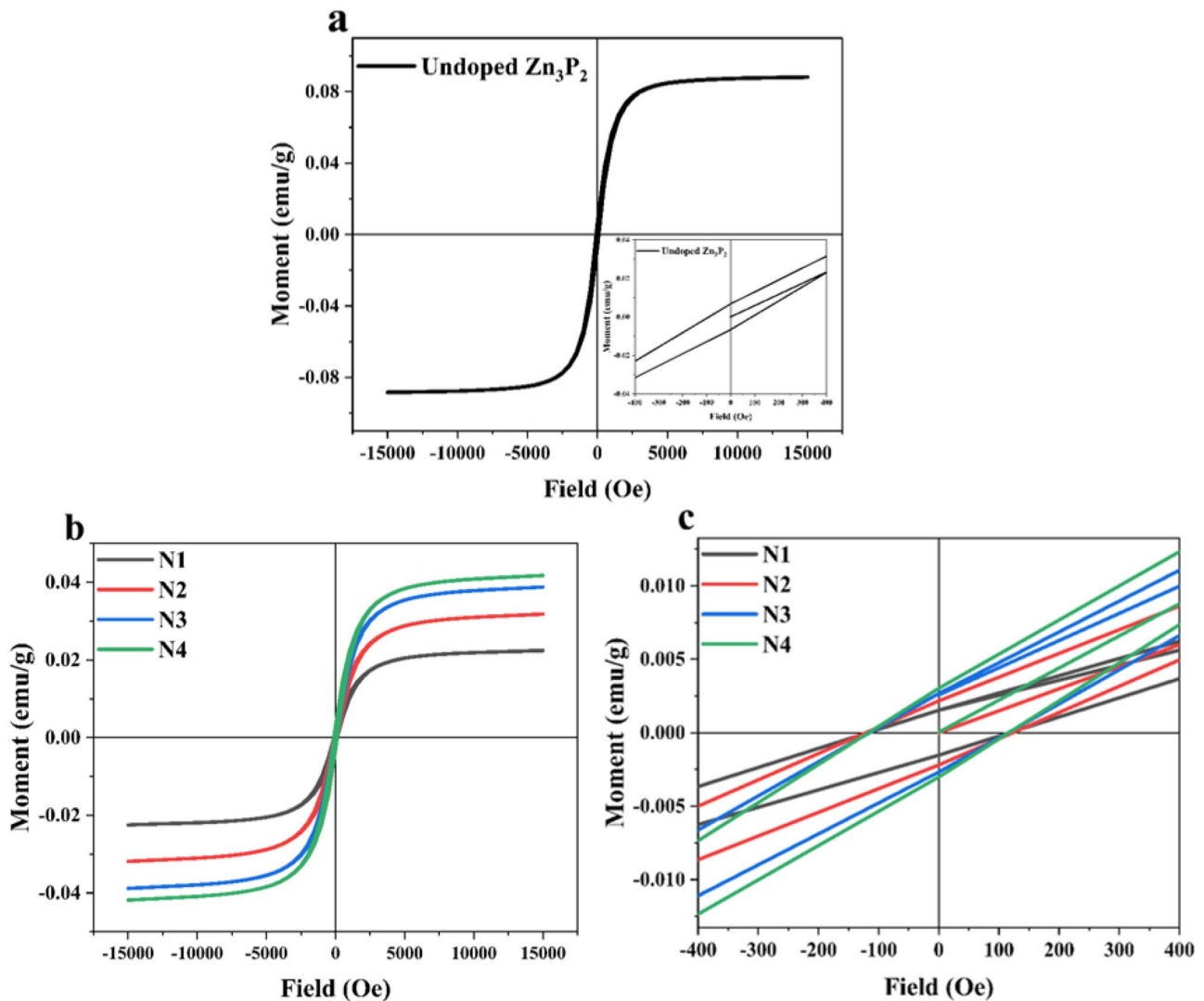


**Fig. 6** M-H loop of  $Zn_3P_2$  (a) Ni-doped  $Zn_3P_2$  (b) nanoparticles in the field range of  $-15,000$  to  $+15,000$  Oe (c) in the field range of  $-400$  to  $+400$  Oe

In a scholarly publication from 2007, V.S. Dang examined the characteristics of  $Zn_3P_2$  when subjected to room temperature conditions. It was determined that  $Zn_3P_2$  remains stable under these conditions and exhibits ferromagnetic properties [46]. The dopant ion, namely  $Ni_2P$ , exhibits ferromagnetic behavior at ambient temperature [47]. The B-H hysteresis loop provides significant data regarding the magnetic behavior of pure and doped samples, specifically in relation to the influence of Ni concentration on magnetic movement. Each sample was evaluated for its saturation magnetization ( $M_s$ ), coercivity ( $H_c$ ), and retentivity ( $M_r$ ), as indicated in Table 2. The three aforementioned factors are contingent upon both the concentration of the dopant and the prevailing temperature. The observed phenomenon is indicative of the magnetic exchange interaction that arises due to variations in the concentration of nickel. The observed magnetic behavior in all doped samples can be attributed to the progressive increase in Ni dopant concentration, ranging from N1 to N4 samples. The lattice of  $Zn_3P_2$  exhibited notable characteristics, including a high saturation magnetization of  $88.295 \times 10^{-3}$  emu/g, a retentivity of  $6.6884 \times 10^{-3}$  emu/g, and a lower coercivity of 89.806 Oe.

Figure 6b presents the magnetization against the applied magnetic field (M-H) curve for nanoparticles of  $Zn_3P_2$  doped with nickel (Ni) throughout the magnetic field range of  $-15,000$  to  $+15,000$  Oe. The sample with a lower concentration of N1 sample exhibited the following magnetic properties: a saturation magnetization of  $22.484 \times 10^{-3}$  emu/g, a coercivity of 117.54 Oe, and a retentivity of  $1.5287 \times 10^{-3}$  emu/g. Furthermore, it was discovered that the saturation magnetization increased as the concentration of Ni increased for the remaining three dopants, namely N2, N3, and N4 samples. The N4 ( $x=0.07$ ) sample shown in Table 2 exhibited the highest saturation magnetization of  $41.819 \times 10^{-3}$  emu/g, a coercivity of 116.56 Oe, and a retentivity of  $3.0217 \times 10^{-3}$  emu/g. The hysteresis loop technique was not employed to compare the transition elements doped in  $Zn_3P_2$ . Instead, multiple researchers conducted investigations on the magnetic characteristics of these elements through the utilization of ab initio studies that relied on density functional theory. In their study, G. Jaiganesh

et al. [25] conducted ab initio investigations to examine the magnetic characteristics of transition elements (V, Cr, Mn, Fe, Co) when doped with  $Zn_3P_2$ . The ferromagnetic phase of a Ti-doped  $Zn_3P_2$  matrix was observed through the utilization of ab initio investigations [23]. Jaiganesh et al. [24] reported that doped cation (Fe) d-like electrons are the primary cause of magnetism. Situated around the Fermi level, the doped cation d-like state is substantially spin-split. Small magnetic moments from the Zn and P atoms are included in the compound's overall magnetic moment ( $4.00 \mu_B$  per unit cell), which is primarily derived from the d-electrons of the doped cation. The effective magnetic moment of the transition elements Ni ( $2.80$ – $3.50 \mu_B$ ) has been experimentally observed [48]. Kai Zeppenfeld et al. [49] reported that  $Ni_2P$  compounds exhibit paramagnetic behavior from 2 to 300 K. To the best of our knowledge, Ni (0.01, 0.03, 0.05, and 0.07) has the most effect on ferromagnetism due to more dopant concentration in the Zn site.

Figure 6c displays the magnetization versus the applied field of nanoparticles composed of Ni-doped  $Zn_3P_2$ . The applied field range spans from  $-400$  to  $+400$  Oe. Table 2 demonstrates the presence of coercivity and retentivity in the pure N1, N2, N3, and N4 samples. At room temperature, an observable shift from weak ferromagnetism (WFM) to ferromagnetism (FM) was noted in the N4 ( $x=0.07$ ) sample, signified by the presence of a perfect ferromagnetism state. Based on the results of this study, it is plausible that the observed findings hold potential utility in the realm of spintronic applications.

## 4 Conclusion

In this study,  $Zn_{3-x}Ni_xP_2$  nanoparticles were synthesized using a typical solid-state reaction approach. The nanoparticles were prepared with four different samples: N1 ( $x=0.01$ ), N2 ( $x=0.03$ ), N3 ( $x=0.05$ ), and N4 ( $x=0.07$ ). The synthesis process was successful in all cases. The specimen underwent analysis to determine its structural, optical, and magnetic characteristics. The findings from X-ray diffraction spectrometer analyses indicate that the nickel dopant concentrations are accurately incorporated within the pure system. Furthermore, the synthesized samples exhibit no additional peaks, suggesting the absence of impurities. Additionally, all the synthesized nanoparticles possess a tetragonal structure, further confirming the absence of impurities. The elemental analysis conducted has proven that the current EDAX spectra do not involve any additional elements and closely approximate the desired atomic ratio. In the field of morphological research, the particles have a tendency to aggregate. The diffused reflectance spectra analyses reveal that the pure sample exhibits its highest reflectance in the infrared (IR)

**Table 2** Parameters of magnetization ( $M_s$ ), coercivity ( $H_c$ ), and retentivity ( $M_r$ ) for pure and Ni-doped  $Zn_3P_2$  nanoparticles at room temperature

$Zn_{3-x}Ni_xP_2$	Magnetization ( $M_s$ ) (emu/g)	Coercivity ( $H_c$ ) (Oe)	Retentivity ( $M_r$ ) (emu/g)
Pure	$88.295 \times 10^{-3}$	89.806	$6.6884 \times 10^{-3}$
N1 ( $x=0.01$ )	$22.484 \times 10^{-3}$	117.54	$1.5287 \times 10^{-3}$
N2 ( $x=0.03$ )	$31.863 \times 10^{-3}$	121.99	$2.1840 \times 10^{-3}$
N3 ( $x=0.05$ )	$38.820 \times 10^{-3}$	115.13	$2.6739 \times 10^{-3}$
N4 ( $x=0.07$ )	$41.819 \times 10^{-3}$	116.56	$3.0217 \times 10^{-3}$

region. As the concentration of the dopant increases, the reflectance increases. Furthermore, the optical band gap experiences an increase in value from 1.410 to 1.433 eV as the dopant concentration increases from N1 to N4 samples. The photoluminescence spectra demonstrated that the emission bands of all the synthesized nanoparticles were observed at nearly identical wavelength positions, despite being excited at varied wavelengths of 210 nm, 215 nm, 240 nm, and 307 nm. The presence of dopant concentration was shown to induce a transition from mild ferromagnetism to ferromagnetism, as validated by the vibrating sample magnetometer.

**Acknowledgements** Very thankful for providing chemicals from RGEMS found. VIT-AP provides UV-vis-NIR Spectroscopy. XRD and SEM with EDAX providing Yogivemana University Kadapa and thanks to Dr. Jayasimhadri for providing PL at Delhi Technological University. Thanks to IIT Madras for providing VSM facilities.

**Data Availability** Data will be made available on reasonable request.

## References

- Chen, W., Buyanova, I.: Handbook of Spintronic Semiconductors. CRC Press (2019)
- Zutic, I., Fabian, J., Sarma, S.D.: Spintronics: fundamentals and applications. Rev. Mod. Phys. **76**, 323 (2004)
- Mauger, A., Godart, C.: The magnetic, optical, and transport properties of representatives of a class of magnetic semiconductors: the europium chalcogenides. Phys. Rep. **141**, 51–176 (1986). [https://doi.org/10.1016/0370-1573\(86\)90139-0](https://doi.org/10.1016/0370-1573(86)90139-0)
- Fukuma, Y., Goto, K., Senba, S., Miyawaki, S., Asada, H., Koyanagi, T., Sato, H.: IV-VI diluted magnetic semiconductor Ge<sub>1-x</sub>Mn<sub>x</sub>Te epilayer grown by molecular beam epitaxy. J Appl Phys **103**, (2008). <https://doi.org/10.1063/1.2871193>
- Ohno, H., Munekata, H., Von Penney, Y.T., Molnar, S., Chang, L.L.: Magnetotransport properties of p-type (In, Mn) As diluted magnetic III-V semiconductors. Phys. Rev. Lett. **68**, 2664 (1992). <https://doi.org/10.1103/PhysRevLett.68.2664>
- Haury, A., Wasiela, A., Arnoult, T.A., Cibert, J., Tatarenko, S., Dietl, T., dAubigne, Y.M.: Observation of a ferromagnetic transition induced by two-dimensional hole gas in modulation-doped CdMnTe quantum wells. Phys Rev Lett **79**, 511 (1997). <https://doi.org/10.1103/PhysRevLett.79.511>
- Dietl, T., Ohno, O.H., Matsukura, A.F., Cibert, J., Ferrand, E.D.: Zener model description of ferromagnetism in zinc-blende magnetic semiconductors. Sci **287**, 1019–1022 (2000). <https://doi.org/10.1126/science.287.5455.1019>
- Soundararajan, D., Mangalaraj, D., Nataraj, D., Dorosinskii, L., Kim, K.H.: Magnetic properties of Cr doped ZnTe alloy powder. Mate. Lett. **87**, 113–116 (2012). <https://doi.org/10.1016/j.matlet.2012.07.042>
- Chaitanya Kumar, K., Madhusudhana Rao, N., Kaleemulla, S., Venugopal Rao, G.: Structural, optical and magnetic properties of Sn doped ZnS nanopowders prepared by solid-state reaction. Phys B Condens **522**, 75–80 (2017). <https://doi.org/10.1016/j.physb.2017.07.071>
- Holub, M., Chakrabarti, S., Fathpour, S., Bhattacharya, P., Lei, Y., Ghosh, S.: Mn-doped InAs self-organized diluted magnetic quantum-dot layers with Curie temperatures above 300K. Appl. Phys. Lett. **85**, 973–975 (2004). <https://doi.org/10.1063/1.1781361>
- Zhang, Y., Liu, W., Niu, H.: Half-metallic ferromagnetism in Cr-doped AIP density functional calculations. Solid state commun. **145**, 590–593 (2008). <https://doi.org/10.1016/j.ssc.2007.12.022>
- Mi, W.B., Jiang, E.Y., Bai, H.L.: Structure, magnetic and optical properties of polycrystalline Co-doped TiO<sub>2</sub> films. J. Magn. Magn. Mater. **321**, 2472–2476 (2009). <https://doi.org/10.1016/j.jmmm.2009.03.017>
- Kuppan, M., Kaleemulla, S., MadhusudhanaRao, N., Regana Sai-Krishna, N., Begam, M., Sreekantha., Reddy, M.: Structural, optical and magnetic properties of Ni-doped SnO<sub>2</sub> thin films prepared by flash evaporation technique. Int J Chem Tech Res **6**, 1933–1935 (2014). <https://doi.org/10.1149/1.2108615>
- Bhushan, M., Turner, J.A., Parkinson, B.A.: Photoelectrochemical investigation of Zn<sub>3</sub>P<sub>2</sub>. J. Electrochem. Soc. **133**, 536 (1986). <https://doi.org/10.1149/1.2108615>
- Villars, P., Calvert, L.D.: Pearson's handbook of crystallographic data for intermediate phases. American Society of Metals, Cleveland, OH (1985)
- Kimball, G.M., Müller, A.M., Lewis, N.S., Atwater, H.A.: Photoluminescence-based measurements of the energy gap and diffusion length of Zn<sub>3</sub>P<sub>2</sub>. Appl. Phys. Lett. **95**, 11 (2009). <https://doi.org/10.1063/1.3225151>
- Yang, R., Chueh, Y.L., Morber, J.R., Snyder, R., Chou, L.J., Wang, Z.L.: Single-crystalline branched zinc phosphide nanostructures: synthesis, properties, and optoelectronic devices. Nano Lett. **7**, 269–275 (2007). <https://doi.org/10.1021/nl062228b>
- Shen, G.: Chen, One-dimensional nanostructures and devices of II–V group semiconductors. Nanoscale Res. Lett. **4**, 779–788 (2009). <https://doi.org/10.1007/s11671-009-9338-2>
- Pawlikowski, J.M.: Comments on Zn<sub>3</sub>P<sub>2</sub> band structure. J. Appl. Phys. **53**, 3639–3642 (1982). <https://doi.org/10.1063/1.331146>
- Stamov, I.G., Syrbu, N.N., Dorogan, A.V.: Energetic band structure of Zn<sub>3</sub>P<sub>2</sub> crystals. Phys. B: Condens. **408**, 29–33 (2013). <https://doi.org/10.1016/j.physb.2012.09.029>
- Pawlikowski, J.M.: Absorption edge of Zn<sub>3</sub>P<sub>2</sub>. Phys. Rev. B **26**, 4711 (1982). <https://doi.org/10.1103/PhysRevB.26.4711>
- Luber, E.J., Mobarok, M.H., Buriak, J.M.: Solution-processed zinc phosphide (α-Zn<sub>3</sub>P<sub>2</sub>) colloidal semiconducting nanocrystals for thin film photovoltaic applications. ACS Nano **7**, 8136–8146 (2013). <https://doi.org/10.1021/nn4034234>
- Sekaran, J.G., Mathi Jaya, S.: Effect of partial Ti substitution at Zn sites on the structural, electronic and magnetic properties of Zn<sub>3</sub>P<sub>2</sub>. Authorea Preprints (2020). <https://doi.org/10.22541/au.160466779.91279508/v1>
- Jaiganesh, G., Mathi Jaya, S.: Half-metallic ferromagnetism in Fe-doped Zn<sub>3</sub>P<sub>2</sub> from first-principles calculations. In AIP Conference Proceedings. Am. Inst. Phys. **1591**, 1081–1083 (2014). <https://doi.org/10.1063/1.4872860>
- Jaiganesh, G., Mathi Jaya, S.: Magnetism, electronic structure and half-metallic property of transition metal (V, Cr, Mn, Fe, Co) substituted Zn<sub>3</sub>P<sub>2</sub> dilute magnetic semiconductors: an ab-initio study. Comput. Mater. Sci. **102**, 85–94 (2015). <https://doi.org/10.1016/j.commatsci.2015.02.018>
- Jaiganesh, G., Mathi Jaya, S.: Electronic structure and magnetism of titanium substituted Cd<sub>3</sub>P<sub>2</sub>: an ab-initio study. AIP Conference Proceedings. AIP Publishing LLC. **1953**, (2018). <https://doi.org/10.1063/1.5033127>
- Laiho, R., Lisunov, K.G., Lähderanta, E., Zakhvalinskii, V.S.: Magnetic properties of the new diluted, magnetic semiconductor: evidence of MnAs clusters. J. Phys. Condens. Matter **11**, 555 (1999). <https://doi.org/10.1088/0953-8984/11/2/018>
- Laiho, R., Lisunov, K.G., Lahderanta, E., Zakhvalinskii, V.S.: Magnetic MnAs nanoclusters in the diluted magnetic semiconductor (Zn<sub>1-x</sub>Mn<sub>x</sub>)<sub>3</sub>As<sub>2</sub>. J. Phys. Condens. Matter **11**, 8697 (1999)
- Denissen, C.J.M., Nishihara, H.V., De Gool, J.C., Jonge, W.J.M.: Magnetic behavior of the semimagnetic semiconductor

- (Cd<sub>1-x</sub>Mn<sub>x</sub>)<sub>3</sub>As<sub>2</sub>. *Phys. Rev. B* **33**, 7637 (1986). <https://doi.org/10.1103/PhysRevB.33.7637>
30. El Zawawi, I.K., Moez, A.A., Hammad, T.R., Ibrahim, R.S.: Phase transformation and disorder effect on optical and electrical properties of Zn<sub>3</sub>P<sub>2</sub> thin films. *Spectrochim. Acta-A: Mol. Biomol.* **94**, 378–383 (2012). <https://doi.org/10.1016/j.saa.2012.03.072>
  31. Jayachandriah, C., Siva Kumar, K., Krishnaiah, G., Rao, N.: Madhusudhana Influence of Dy dopant on structural and photoluminescence of Dy-doped ZnO nanoparticles. *J. Alloys. Compound.* **623**, 248–254 (2015). <https://doi.org/10.1016/j.jallcom.2014.10.067>
  32. Kuppan, M., Kaleemulla, S., Madhusudhana Rao, N., Sai Krishna, N., Rigana Begam, M., Shobana, M.: Structural and magnetic properties of Ni-doped Adv. *Condens. Matter. Phys.* (2014). <https://doi.org/10.1155/2014/284237>
  33. Cullity, B.D.: *Elements of X-Ray diffraction*. Addison-Wesley, Reading, Mass, USA (1972)
  34. Jothibas, M., Manoharan, C., Jeyakumar, S.J., Praveen, P., Punithavathy, I.K., Richard, J.P.: Synthesis and enhanced photocatalytic property of Ni doped ZnS nanoparticles. *Solar Energy* **159**, 434–443 (2018). <https://doi.org/10.1016/j.solener.2017.10.055>
  35. Stolterfoht, M., Wolff, C.M., Marquez, J.A., Zhang, S., Hages, C.J., Rothhardt, D., Neher, D.: Visualization and suppression of interfacial recombination for high-efficiency large-area pin perovskite solar cells. *Nat. Energy* **3**, 847–854 (2018)
  36. Misiewicz, J.: Inter-band transitions in Zn<sub>3</sub>P<sub>2</sub>. *J. Condens. Matter phys.* **2**, 2053 (1990). <https://doi.org/10.1088/0953-8984/2/8/012>
  37. Kimball, G.M., Muller, A.M., Lewis, N.S., Atwater, H.A.: Photoluminescence-based measurements of the energy gap and diffusion length of Zn<sub>3</sub>P<sub>2</sub>. *Appl. Phys. Lett.* **95**, 112103 (2009). <https://doi.org/10.1063/1.3225151>
  38. Suresh Babu, V., Vaya, P.R.: Photoluminescence properties of doped and unintentionally doped hot wall deposited polycrystalline Zn<sub>3</sub>P<sub>2</sub> films. *Microelectron. J.* **21**, 35–40 (1990). [https://doi.org/10.1016/0026-2692\(90\)90006-O](https://doi.org/10.1016/0026-2692(90)90006-O)
  39. Ho, M.Q., Esteves, R.J.A., Kedarnath, G., Arachchige, I.U.: Size-dependent optical properties of luminescent Zn<sub>3</sub>P<sub>2</sub> quantum dots. *J. Phys. Chem. C* **119**, 10576–10584 (2015). <https://doi.org/10.1021/acs.jpcc.5b01747>
  40. Poornaprakash, B., Amaranatha Reddy, D., Murali, G., Madhusudhana Rao, N., Vijayalakshmi, R.P., Reddy, B.K.: Composition dependent room temperature ferromagnetism and PL intensity of cobalt doped ZnS nanoparticles. *J. Alloys Compd.* **577**, 79 (2013). <https://doi.org/10.1016/j.jallcom.2013.04.106>
  41. Shen, G.Z., Bando, Y., Hu, J.Q., Golberg, D.: Single-crystalline trumpetlike zinc phosphide nanostructures. *Appl. Phys. Lett.* **88**, 143105 (2006). <https://doi.org/10.1063/1.2192090>
  42. Lim, T.H., Teh, G.B., Tilley, R.D.: Synthesis and characterization of highly crystalline zinc phosphide nanoparticles. *Key Eng. Mater.* **701**, 3–7 (2016). <https://doi.org/10.4028/www.scientific.net/KEM.701.3>
  43. Qiu, D.J.Wu., Feng, H.Z., Lao, A.M., Chen, Y.F., Xu, N.B., T. N.: Annealing effects on the microstructure and photoluminescence properties of Ni-doped ZnO films. *Appl. Surf. sci.* **222**, 263–268 (2004). <https://doi.org/10.1016/j.apsusc.2003.08.015>
  44. Tong, L.N., Cheng, T., Han, H.B., Hu, J.L., He, X.M., Tong, Y., Schneider, C.M.: Photoluminescence studies on structural defects and room temperature ferromagnetism in Ni and Ni-H doped ZnO nanoparticles. *J. App. Phys.* **108**, (2010). <https://doi.org/10.1063/1.3460644>
  45. Kaur, P., Kumar, S., Chen, C.L., Yang, K.S., Wei, D.H., Dong, C.L., Srivastava, C., Rao, S.M.: Gd doping induced weak ferromagnetic ordering in ZnS nanoparticles synthesized by low-temperature co-precipitation technique. *Mater. Chem. Phys.* **186**, 124–130 (2017). <https://doi.org/10.1016/j.matchemphys.2016.10.037>
  46. Yoo, Y.G.: Ferromagnetism-to-paramagnetism transition in the ZnMnO system. *J. Korean Phys. Soc.* **52**, 1398–1401 (2008)
  47. Zhang, D., Zhou, X., Liu, J., Dong, L., Zhao, J., Xie, Y., Sun, W.: Selective synthesis of Ni<sub>12</sub>P<sub>5</sub> and Ni<sub>2</sub>P nanoparticles: electronic structures, magnetic and optical properties. *Mater. Sci. Eng. B* **273**, 115389 (2021). <https://doi.org/10.1016/j.mseb.2021.115389>
  48. Ferenc, W., Dariusz, O., Sarzyński, J., Gluchowska, H.: Complexes of Mn (II), Co (II), Ni (II), Cu (II) and Zn (II) with ligand formed by condensation reaction of isatin with glutamic acid. *Ecletica Química* **45**, 12–27 (2020). <https://doi.org/10.26850/1678-4618eqj.v45.3>
  49. Zeppenfeld, K., Jeitschko, W.: Magnetic behaviour of Ni<sub>3</sub>P Ni<sub>2</sub>P, NiP<sub>3</sub> and the series Ln<sub>2</sub>Ni<sub>12</sub>P<sub>7</sub> (Ln= Pr, Nd, Sm, Gd-Lu). *J. Phys. Chem. Solids* **54**, 1527–1531 (1993)

**Publisher's Note** Springer Nature remains neutral with regard to jurisdictional claims in published maps and institutional affiliations.

Springer Nature or its licensor (e.g. a society or other partner) holds exclusive rights to this article under a publishing agreement with the author(s) or other rightsholder(s); author self-archiving of the accepted manuscript version of this article is solely governed by the terms of such publishing agreement and applicable law.